Modeling photoelectron transport in the Martian ionosphere at Olympus Mons and Syrtis Major: MGS observations

S. A. Haider,[1] S. P. Seth,[2] D. A. Brain,[3] D. L. Mitchell,[3] T. Majeed,[4,5] and S. W. Bougher[4]

Received 6 October 2009; revised 25 December 2009; accepted 22 February 2010; published 18 August 2010.

[1] We have calculated photoelectron flux, ion production rates, and electron densities in the Martian ionosphere close to Syrtis Major and Olympus Mons at coordinates 5°N, 30°E and 15°N, 210°E, respectively. In the regions of Olympus Mons and Syrtis Major the magnetic fields are horizontal and vertical, respectively. These calculations are made at solar zenith angle 78° during moderate solar activity using transport and local loss models of photoelectrons based on the yield spectrum method. The vertical transport of photoelectrons is inhibited by horizontal magnetic fields at Olympus Mons. In this case we have used a local loss calculation. Photoelectron transport is allowed in the vertical magnetic fields at Syrtis Major. In this case we have developed and applied a photoelectron transport model. The estimated ion production rates are then used in a one-dimensional continuity and vertical diffusion model to calculate ion and electron density. It is found that photoelectron transport reduces the flux by an order of magnitude between energy range 1 to 20 eV at higher altitude (>250 km). In this region the production rates and densities are decreased by factors of 2.5 to 5 due to transport of photoelectrons.

Citation: Haider, S. A., S. P. Seth, D. A. Brain, D. L. Mitchell, T. Majeed, and S. W. Bougher (2010), Modeling photoelectron transport in the Martian ionosphere at Olympus Mons and Syrtis Major: MGS observations, *J. Geophys. Res.*, *115*, A08310, doi:10.1029/2009JA014968.

1. Introduction

[2] The first theoretical study of photoelectron impact ionization at Mars was reported by *Mantas* and *Hanson* [1979] using a time-independent Boltzmann equation. They calculated photoelectron fluxes for both horizontal and vertical magnetic fields and suggested that these limiting cases would be appropriate at Martian equator and poles, respectively, similar to Earth's atmosphere. *Fox and Dalgarno* [1979] have used discrete energy loss processes to study the ionization, luminosity, and heating of the atmosphere of Mars. They reached similar conclusions to those of *Mantas* and *Hanson* [1979] without the inclusion of magnetic field in their model. This global scenario is now changed after Mars Global Surveyor (MGS) observations of strong crustal magnetic fields [*Acuna et al.*, 1998]. The horizontal field assumption is appropriate at both low- and high-latitude regions, whereas the vertical field assumption is appropriate only in regions of crustal magnetic anomalies [cf. *Frahm et al.*, 2006].

[3] In the present paper we have calculated photoelectron flux, production rates and densities in the Martian ionosphere close to Olympus Mons and Syrtis Major at coordinates 15°N, 210°E and 5°N, 30°E, respectively. These calculations are made at solar zenith angle (SZA) 78° under spring equinox and medium solar activity condition. In the region of Olympus Mons the magnetic fields are horizontal in direction and we have used a two-dimensional yield spectrum model. In this case photoelectrons lose their energy at the same altitude they are produced under a local loss approximation. In the region of Syrtis Major the magnetic fields are mostly vertical in direction and we have used a three-dimensional yield spectrum model where vertical transport is allowed. In this case photoelectrons travel some distance before they lose their energy in the Martian atmosphere. These models are based on Monte Carlo simulation. In this technique monoenergetic electrons of different incident energies were introduced into a gas medium with random pitch angle. This method includes elastic and inelastic collisions between electrons and neutral species, continuous energy losses due to Coulomb forces between electrons and ambient thermal electrons, and the Lorentz motion of the electrons around the magnetic fields. These models are

[1]Space and Atmospheric Sciences, Physical Research Laboratory, Ahmedabad, India.
[2]Department of Physics, Bhavan's R. A. College of Science, Gujarat University, Ahmedabad, India.
[3]Space Sciences Laboratory, University of California, Berkeley, California, USA.
[4]Department of Atmospheric, Oceanic and Space Sciences, University of Michigan, Ann Arbor, Michigan, USA.
[5]Now at Department of Physics, American University of Sharjah, Sharjah, United Arab Emirates.

0148-0227/10/2009JA014968

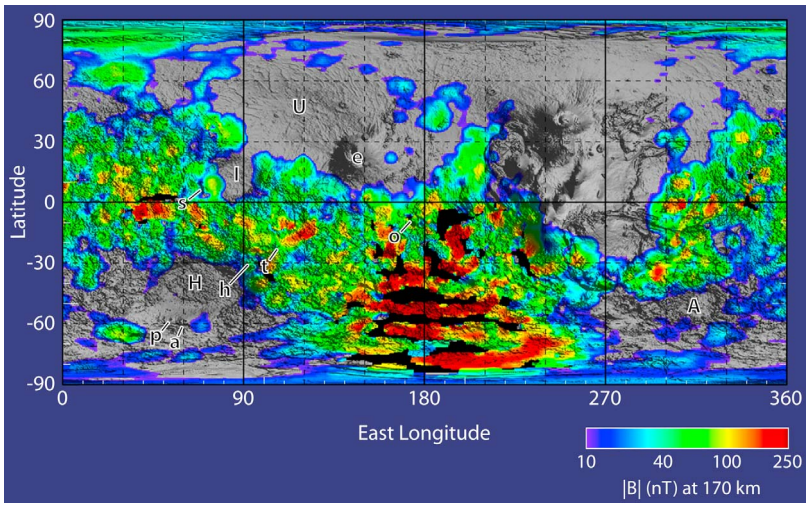

Figure 1. Global map of the crustal magnetic field amplitude (B) of Mars at an altitude 170 km as inferred from electron reflectometry represented by colors superposed on a shaded relief map of MGS Mars Orbiter Laser Altimeter topography. Labels indicate the centers of the Utopia (U), Hellas (H), Argyre (A), and Isidis (I) impact basins, as well as the volcanoes Elysium (e), Syrtis Major (s), Apollinaris (o), Tyrrhena (t), Hadriaca (h), Peneus (p), Amphitrites (a), and Olympus Mons by thick black region, where magnetic field lines are shown from closed loops.

described in section 3. It is found that the transport of photoelectrons is appreciable above 200 km. Photoelectron transport reduces the flux, ion production rates, and densities by factors of 3 to 10 compared to local losses. Hence it is necessary to include transport processes when modeling the low latitude ionosphere where crustal magnetic fields are vertical.

[4] The middle- and high-latitude ionospheres have been observed from past radio science experiments onboard Mariner 4 [*Kliore et al.*, 1965; *Fjeldbo et al.*, 1966]; Mariner 6 and 7 [*Fjeldbo et al.*, 1970]; Mars 2 [*Kolosov et al.*, 1976]; Mariner 9 [*Kliore et al.*, 1972, 1973]; Mars 4, 5, and 6 [*Vasiliev et al.*, 1975; *Savich and Samovol*, 1976]; and Viking 1 and 2 [*Fjeldbo et al.*, 1977] and recently by MGS [*Hinson et al.*, 1999; *Tyler et al.*, 2001] and Mars Express [*Patzold et al.*, 2005]. The ionosphere of Mars has not been observed at low latitude (<30°). The thermospheric density is observed at low latitude by the Accelerometer (ACC) experiment onboard MGS [*Keating et al.*, 1998]. Because of the low pressures above 100 km, ionized species do not necessarily recombine quickly and there is a permanent population of ions and electrons. Although the electron concentration may amount to only ~1% of the neutral concentration the presence of these electrons can have a profound effect on the properties and behavior of the low-latitude ionosphere. The ionosphere also affects radio waves and as a plasma it can support and generate a variety of waves, interactions, and instabilities that are not found in the neutral gas. In absence of ionospheric measurements at low latitude of Mars our model results can be used as a diagnostic tool for future design of payloads and for subsequent data analysis of the ionosphere.

2. Magnetic Fields Over Mars: MGS/MAG data

[5] The first indication of the weakness of the magnetic field of Mars was obtained by the Mariner 4 spacecraft in 1965 [*Smith et al.*, 1965]. Most subsequent magnetic field measurements in the vicinity of Mars were carried out on a series of five Mars spacecraft (Mars 2, 3, 5, 6, and 7) between 1971 and 1974 [*Dolginov et al.*, 1973, 1978a, 1978b]. However, none of these spacecraft approached Mars closer than ~1300 km or ~1.3 Mars radii from center of the planet, and none probed the solar wind wake inside the optical shadow, where the magnetotail of an intrinsic magnetosphere resembling a weak version of Earth's would be found. The Viking Landers reached the surface of Mars in 1976 but did not carry the magnetic field experiment [*Snyder and Moroz*, 1992]. Phobos 2 went into the deep wake of Mars providing magnetic field data in optical shadow at distances as close as ~2.7 Mars radii and as distant as ~20 Mars radii. These data showed that the magnetic fields in the wake of Mars are determined by interplanetary field orientation and are thus not Earth-like at least in the near equatorial orbit plane [*Riedler et al.*, 1989].

[6] In situ measurement of the magnetic field in the upper atmosphere was made by a magnetometer (MAG) onboard MGS. Magnetic fields as high as 400 nT at 108–113 km altitude in the Northern Hemisphere and 1500 nT at 120–200 km altitude in some locations of the Southern Hemisphere were observed from this spacecraft [*Acuna et al.*, 1998; *Connerney et al.*, 1999]. However, the strength of the magnetic fields in other locations at the same altitude range is much lower about 5–15 nT. These magnetic fields are so weak that they do not significantly contribute to the solar wind-Mars interaction. Thus, the solar wind interaction with Mars outside of the crustal magnetic field region should be induced like Venus. As a consequence, solar wind dynamic pressure nearly permanently compresses the interplanetary magnetic field (IMF) into the Martian ionosphere down to 180 km by several orders of magnitude [*Shinagawa and Cravens*, 1989]. In Figure 1 we show a global map from *Mitchell et al.* [2007] of the crustal mag-

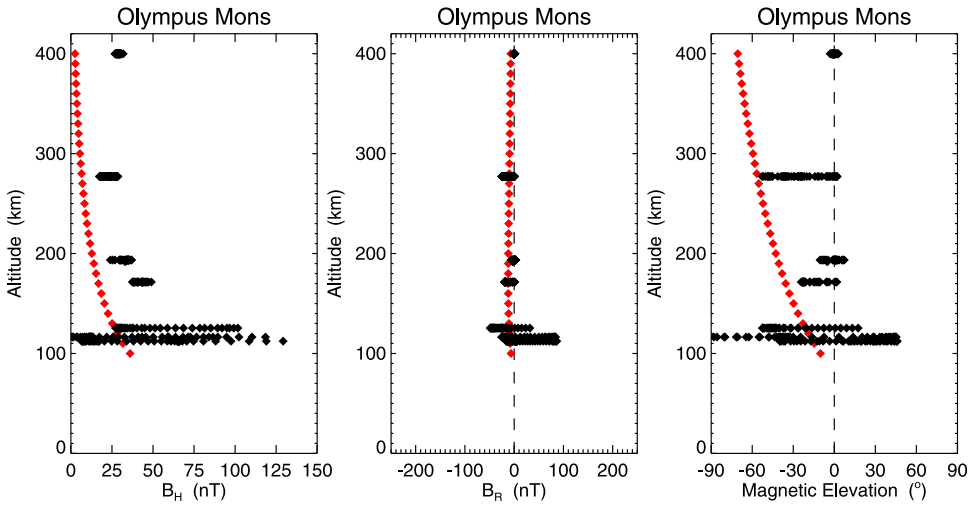

Figure 2. Altitude profiles of magnetic field components (B_R, B_H and elevation angle) in the dayside ionosphere of Mars over Olympus Mons. Cain's model predictions are also shown by red dots lines.

netic field amplitude over Mars at an altitude of ~170 km. The map is derived using an electron reflectometry technique [*Lillis et al.*, 2004] applied to more than two Martian seasons (April 1999 to November 2003) of MGS/MAG and Electron Reflectometer (ER) measurements obtained at altitude of ~400 km and local time of 2 A.M. on the night side of the planet. This technique can probe only magnetic field lines that are connected to the IMF. The maximum and minimum field strengths are 250 nT and 10 nT, respectively. The crustal fields are stronger in the heavily cratered (and thus older) Southern Hemisphere than in the sparsely cratered (younger) Northern Hemisphere [*Connerney et al.*, 2005; *Mitchell et al.*, 2007]. *Brain et al.* [2003] has reported that weak crustal fields extend above 120 km altitude (near the expected altitude of the main ionospheric peak) over ~70% of the surface. The strongest crustal fields extend above 1000 km altitude over some locations of the southern surface (e.g., 140°E to 240°E). We have selected two regions close to Olympus Mons (15°N, 210°E) and Syrtis Major (5°N, 30°E) to study the photoelectron flux, ion production rate, and densities in the Martian ionosphere.

[7] In Figures 2 and 3 the altitude profiles of horizontal and vertical components, B_H and B_R of the magnetic field B measured by MGS, are represented above the two regions (B is equal to the square root of the sum of B_H^2 and B_R^2). The elevation angle of the magnetic field with respect to the local horizontal is also shown in Figures 2 and 3. The positive and negative sign of B_R and elevation angle represent the upward and downward directions of the magnetic field lines, respectively. These profiles are obtained in the dayside atmosphere from MAG data over Olympus Mons (210°–215°E, 10°–20°N) and Syrtis Major (24°–30°E, 6°–12°N). The data in each region were sampled at a variety of local times for solar zenith angles <90°. The maximum value of

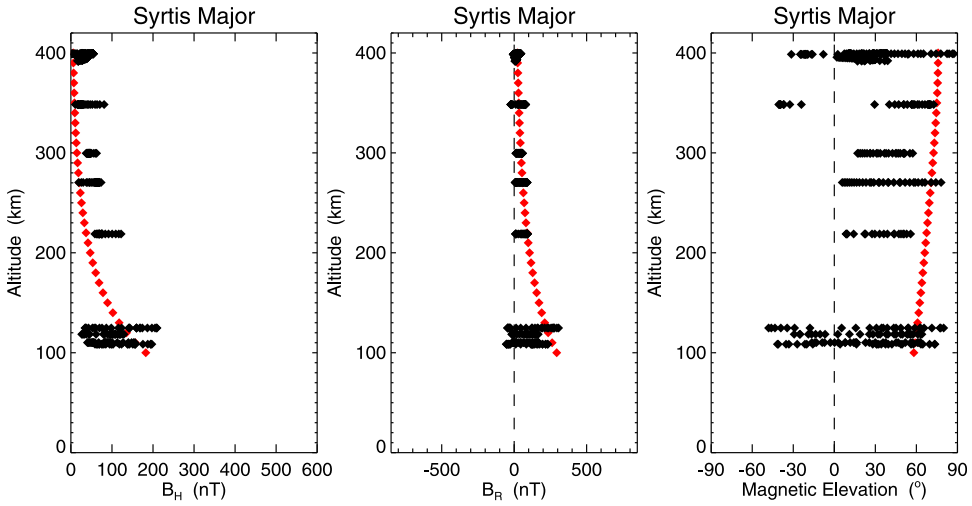

Figure 3. Altitude profiles of magnetic field components (B_R, B_H and elevation angle) in the dayside ionosphere of Mars over Syrtis Major. Cain's model predictions are also shown by red dotted lines.

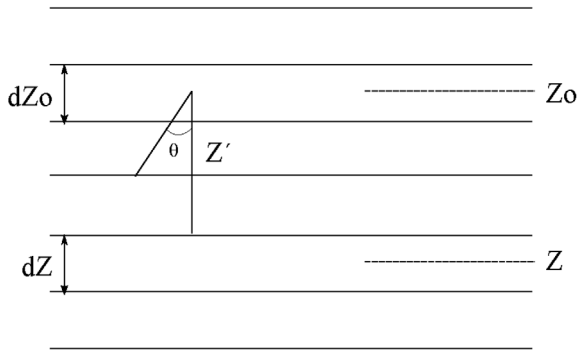

Figure 4. Schematic of division of the Martian atmosphere into slabs.

horizontal magnetic field of ~125 nT is measured at 112 km over Olympus Mons. Above 150 km the vertical field is nearly zero while the horizontal field is observed to be ~25–50 nT. Similarly the highest value of vertical magnetic field of 400 nT is observed at ~112 km over Syrtis Major. Above ~150 km the vertical magnetic fields are larger by a factor of 1.5 than the horizontal magnetic fields. The crustal magnetic field strength decreases rapidly in the Martian ionosphere above 112 km. It should be noted that the external magnetic field effects are also present in these measurements. Therefore the actual magnetic field lines cannot be vertical at the top of the ionosphere, where the solar wind has a strong influence. However, the magnetic fields are horizontal and vertical at most of the altitudes in the upper atmosphere of Olympus Mons and Syrtis Major, respectively. This scenario can be changed at other locations of Mars.

[8] In Figures 2 and 3 we have also shown altitude profiles from the crustal magnetic model of *Cain et al.* [2003]. The Cain model predictions are shown for the central latitude and longitude in each region. There is a good agreement between calculation and measurements in vertical field components over the two regions. In these regions the measured values of B_H are larger than the calculations because of the presence of the external magnetic fields of solar wind in the MAG data. The elevation angles ≤0 and >0 represent that the magnetic fields are horizontal and vertical in downward and upward directions over Olympus Mons and Syrtis Major, respectively. The *Cain et al.* [2003] crustal field model has a reasonable accuracy where external fields are minimized [*Brain et al.*, 2003]. It predicts the radial field component better than the horizontal field component. This is expected since the external fields, draped around the planet on the dayside, influence the radial component least. The magnitude of the field is larger in the measurements than in the model prediction because the model does not include an external field contribution. This is supported by the fact that the average difference between the data and model is largest in the horizontal field component magnitudes.

3. Yield Spectrum Model

[9] This model calculates the energy degradation of ≤1000 eV electrons in the atmosphere of Mars using a Monte Carlo approach. The energy of secondary or tertiary electrons and their positions are calculated at that time when primary electrons ionize the atmospheric gases. In this way a yield spectrum function was generated for the calculation of the yield of any state in the mixture of gases. This method has been represented in terms of two-, three-, four-, and five-dimensional functions. These functions are fitted analytically later. This method has been widely used by earlier workers in problems dealing with energetic degradation in gases and in applications to planetary atmospheres [*Green et al.*, 1977; *Singhal et al.*, 1980; *Singhal and Green*, 1981; *Haider and Singhal*, 1983; *Singhal and Haider*, 1984, *Seth et al.*, 2002, 2006a, 2006b; *Bhardwaj and Jain*, 2009]. In this paper we have used two- and three-dimensional yield spectrum methods as given below.

3.1. Three-Dimensional Yield Spectrum: Transport Model

[10] We recently used the three-dimensional yield spectrum model to study the ion production rates owing to precipitation of solar wind electron in the nighttime ionosphere of Mars [*Haider et al.*, 2007]. We have extended this model to calculate the photoelectron transport flux and production rates in presence of vertical crustal magnetic fields at Syrtis Major. To develop this model we have divided the atmosphere of Mars into slabs as shown in Figure 4. Let the area of cross section of each slab be A. We wish to obtain the photoelectron flux/production rate at height h. Consider a slab of thickness dh_o at h_o. The total number of primary photoelectrons in the energy interval between E_o and E_o+dE_o is $Q(h_o,E_o)\,dE_o\,Adh_o$, where $Q(h_o, E_o)$ is the primary photoelectron production rate at height h_o and incident energy E_o. Since the photoelectrons are emitted isotropically, the number with direction lying between θ and $\theta+d\theta$ will be given by $Q(h_o,E_o)\,dE_o\,Adh_o\,\sin\theta d\theta/2$. The number of inelastic events of type j in gas i produced in the slab of thickness dh at h due to these primary photoelectrons will be given as

$$\text{Number of events} = \int_{w_{ki}}^{1000} dE_o \int_{w_{ki}}^{E_o} p_{ki}(E)\,dE \int_0^{\pi} \frac{Q(h_o,E_o)}{2} A\,dh_o \sin\theta\; U^c(E,Z,E_o)\;\frac{dh}{\cos\theta}\;d\theta. \tag{1}$$

The differential volume ion production rate at height h is obtained by dividing $A\,dh$ as

$$\frac{dP}{dh} = \int_{w_{ki}}^{1000} dE_o \int_{w_{ki}}^{E_o} p_{ki}(E)\,dE \int_0^{\pi/2} \frac{Q(h_o,E_o)}{2} dh_o\, U_f^c(E,Z,E_o) \cdot \frac{\rho(h)}{\cos\theta}\sin\theta\,d\theta + \int_{w_{ki}}^{1000} dE_o \int_{w_{ki}}^{E_o} p_{ki}(E)\,dE \int_{\pi/2}^{\pi} \frac{Q(h_o,E_o)}{2} \cdot dh_o\, U_b^c(E,Z,E_o)\;\frac{\rho(h)}{\cos\theta}\sin\theta\,d\theta. \tag{2}$$

The integration of equation (2) over dh_o will give the ion production rates $P(h)$ at height h due to all photoelectrons produced in other slabs. Finally, changing the order of

integration of dE and dE_o and comparing with the following equation of the production rate $V(h)$ as

$$V(h) = n_i \int_{w_{ki}}^{1000} \phi(h,E)\ \sigma_{ki}(E)\ dE \tag{3}$$

we get

$$\varphi(h,E) = \int \frac{dh_o \rho(h)}{\sum n_j \sigma_j(E)} \int_E^{1000} \frac{Q(h_o,E_o)}{2} dE_o\ X \cdot \left\{ \int_o^{\pi/2} U_f^c(E,Z,E_o)\ \tan\theta\, d\theta + \int_{\pi/2}^{\pi} U_b^c(E,Z,E_o)\ \tan\theta\, d\theta \right\}. \tag{4}$$

In the above equation variable Z depends on altitude h by following relation:

$$Z(h) = \frac{1}{R}\int_0^{\infty} \frac{\rho(h)}{\cos\theta} d\,h, \tag{5}$$

where p_{ki} is the probability for ionizing kth state of gas i as

$$p_{ki}(E) = \frac{n_i\ \sigma_{ki}(E)}{\sum n_j\ \sigma_j(E)}. \tag{6}$$

Here σ_{ki} is the cross section, w_{ki} is the threshold energy for ionization, E is the energy of ejected photoelectron, and n_i is neutral density. R is a scale factor. The scale factor for N_2 and O are given by *Singhal et al.* [1980] and *Singhal and Green* [1981]. These parameters are not changing significantly for different gases and the yield spectrum has almost universal character. However, the scale factor for gas i and j are related as

$$\frac{R_i}{R_j} = \frac{m_i}{m_j}\left\langle \frac{\sigma_{Tj}(E)}{\sigma_{Ti}(E)} \right\rangle, \tag{7}$$

where $\sigma_{Tj}(E)/\sigma_{Ti}(E)$is the average value of the total (elastic + inelastic) cross section and m is the mass of atom or molecule. This relation is used to construct the yield spectra for CO_2, N_2, O_2, O, and CO. The primary photoelectron spectrum $Q(h_o, E_o)$ is calculated at SZA 78° using generalized Chapman function as given by *Seth et al.* [2006a, 2006b]. $\rho(h)$ is the mass density. $U^c_f(E, Z, E_o)$ and $U^c_b(E, Z, E_o)$ are three-dimensional composite yield spectra for forward and backward directions, respectively [*Singhal and Haider*, 1984; *Haider and Singhal*, 1986]. The yield spectra represent the energy spectrum of all the photoelectrons in the medium. The function for $Z \geq 0$ represents the forward photoelectron spectra while for $Z < 0$ represents the backward photoelectron spectra. The composite yield spectra for a mixture of gases are obtained by weighting the component of the yield spectrum as given below:

$$U_f^c(E,Z,E_o) = \sum_i f_i\ U_{fi}\ (E,Z,E_o). \tag{8a}$$

$$U_b^c(E,Z,E_o) = \sum_i f_i\ U_{bi}(E,Z,E_o). \tag{8b}$$

3.2. Two-Dimensional Yield Spectrum: Local Loss Approximation

[11] Following *Haider et al.* [2009] we have calculated the photoelectron flux and impact ionization rates at Olympus Mons in the presence of horizontal magnetic field as given below:

$$J(h) = \int_{w_{ki}}^{1000} dE_o \int_E^{1000} p_{ki}(E)\ Q(h_o,E_o) U^c(E,E_o)\ dE, \tag{9}$$

where $J(h)$ is the photoelectron production rate at altitude h and $U^c(E,E_o)$ is the two-dimensional composite yield spectrum, which is obtained by weighting the component of the yield spectrum $U(E,E_o)$ as

$$U^c(E,E_o) = \sum_i f_i\ U_i(E,E_o). \tag{10}$$

Comparing equations (9) and (3) we get the expression for photoelectron flux in the presence of a horizontal crustal magnetic field as given below:

$$\varphi(h,E) = \int_E^{1000} \frac{Q(h_o,E_o) U^c(E,E_o)}{\sum n_j\ \sigma_j(E)} dE_o. \tag{11}$$

4. Neutral Density and MGS/ACC Data

[12] We have derived neutral densities of five gases (CO_2, N_2, O_2, O, and CO) from mass density, which was measured by the MGS/ACC experiment between 110 and 160 km altitudes at latitude range 0° N to 25°N in phase 2 aerobraking of the MGS mission during orbits P790 to P910 for a 1-month period in December 1998. At that time Mars had summer season (Ls = 90) with moderate solar activity period ($F_{10.7}$ = 124). Within these orbits, the mass densities are distributed fairly well at about all longitudes. The mass density is later multiplied by mixing ratios of CO_2, N_2, O_2, O, and CO to obtain their neutral densities. The mixing ratios of these gases are taken from *Bougher et al.* [2000] and *Fox* [1997] at different altitudes for similar conditions of measurement. No significant variation is found in the mixing ratios with east longitude. The derived neutral densities are used in the calculations of photoelectron flux, production rates, and ion/electron density. Beyond 160 km, the mass density is not measured by ACC. Therefore the neutral density above this altitude is also taken from *Bougher et al.* [2000] and *Fox* [1997]. We have used the

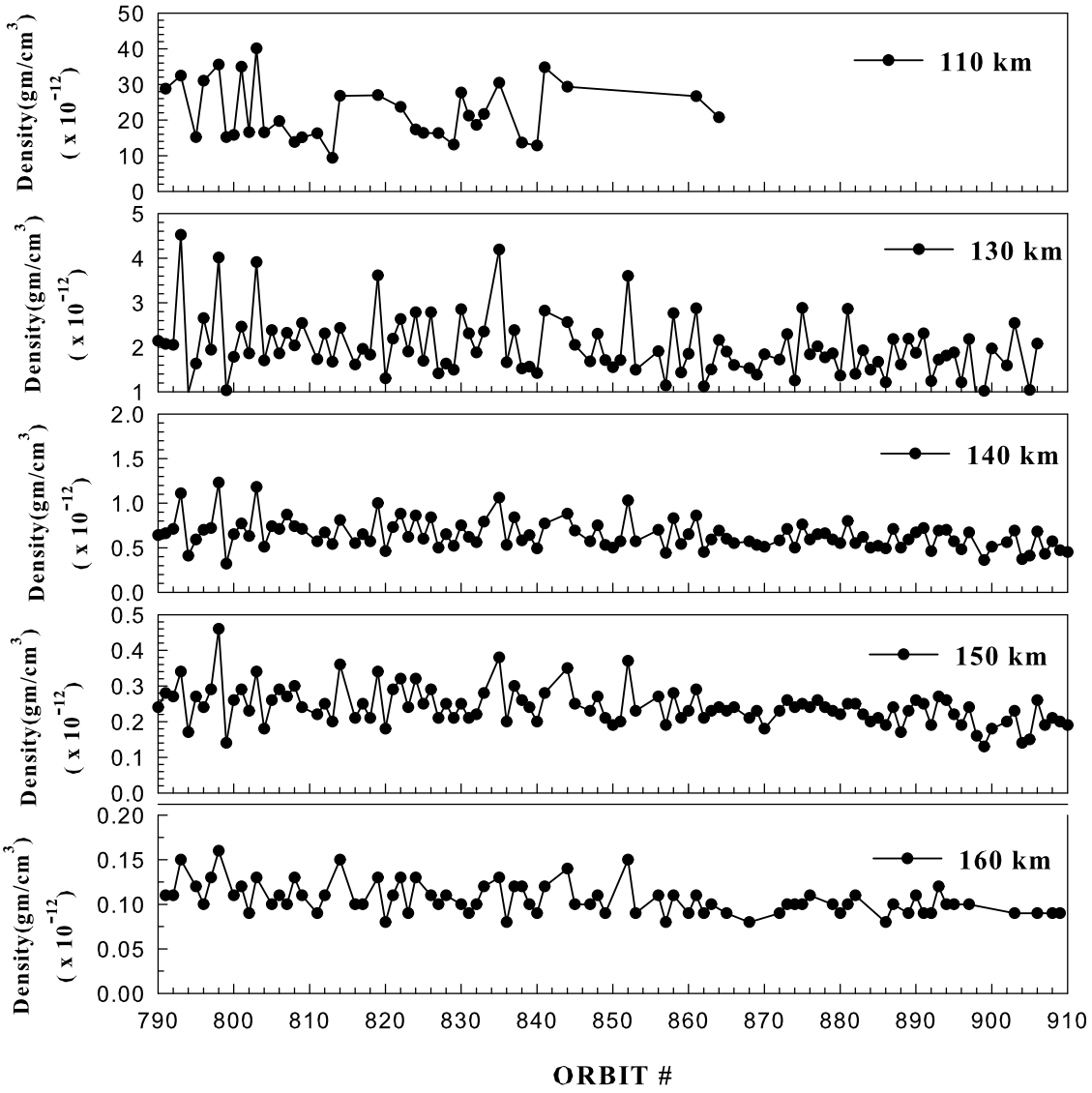

Figure 5. MGS/ACC measurements of mass densities for different orbits are plotted at altitudes 110–160 km between latitudes 0°–25°N and longitudes 0°–360°E.

solar 2000 model to obtain the solar flux during this period [*Tobiska et al.*, 2000]. This model is binned into 73 wavelength intervals. The solar flux is scaled by $1/R^2$ where R is Mars' heliocentric distance (equal to 1.653 AU), appropriate for ACC measurements. The branching ratio, photo absorption, and photoionization cross sections are taken from *Haider and Oyama* [2002]. We have constructed model atmospheres in the regions of Olympus Mons (15°N, 210°E) and Syrtis Major (5°N, 30°E) at different altitudes from 110 km to 350 km using intervals of 1.0 km. Linear interpolation is used wherever ACC data are not available at these intervals. The height distributions of photoelectron flux and impact ionization rates are calculated using these model atmospheres. To save computational time for the calculation of photoelectron flux/impact ionization rates, we have chosen energy grids of width 1 eV for 1–10 eV; 2.5 eV for 10–50 eV; 5 eV for 50–100 eV and 25 eV for 100–1000 eV.

[13] In Figure 5 we show the orbital distribution of mass densities at several altitudes (110,130,140,150 and 160 km) at a low-latitude region (0°N–25°N). These densities are measured by the MGS/ACC experiment at SZA 78° for various inbound legs of 120 orbits. More data are available for the inbound portions of the orbit than the outbound portions. There is a little difference in longitude structure of the inbound and outbound density fields, suggesting a fairly steady wave structure [*Keating et al.*, 1998]. Therefore we have taken densities in our model from various inbound orbits. The data are not available at 110 km between orbits P866 and P910. There is a large variation in mass densities near spacecraft periapsis at 130 km. The variability in mass densities decreases with altitude and little variability is evident at altitudes beyond 160 km. There is little variation in densities in orbits P865 to P910 relative to that observed between orbits P790 and P864. In Figure 6 we illustrate the longitudinal density distribution of the major gas CO_2 measured in 120 orbits at the same altitudes as shown in Figure 5 (the longitudinal density distribution of other gases viz. N_2, O_2, O, and CO are not plotted because of their low

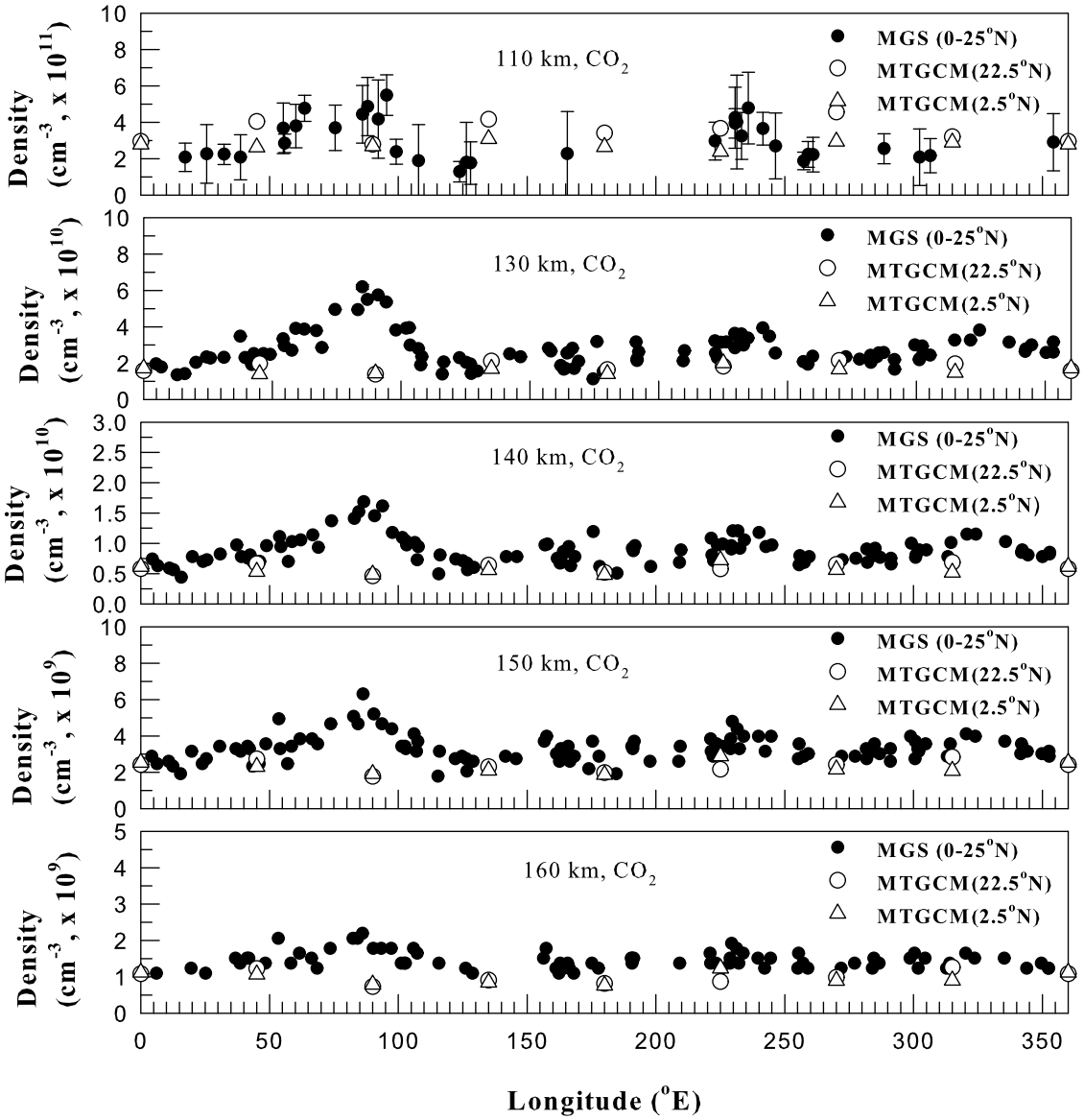

Figure 6. The longitudinal densities of CO_2 are plotted at same altitudes, latitudes and longitudes as shown in Figure 5. MTGCM results for CO_2 are also represented at latitudes 2.5°N and 22.5°N.

values). The measured densities are compared with results from the Mars Thermosphere Global Circulation Model (MTGCM), which were carried out at two northern latitudes 2.5°N and 22.5°N. There are no significant differences between these calculations made for the two latitudes. Thus, the Martian thermosphere does not change significantly at low latitudes. The observed density is enhanced by factor of ~2 to 3 near 80°E as compared to that measured at other eastern longitudes. This is possibly due to the influence of a strong regional dust storm. The Mars Orbiter Camera onboard MGS has measured many local and regional dust storm events from Mars in the month of December 1999 at low and middle latitudes [cf. *Cantor et al.*, 2001]. Based on these measurements, local dust storms are confined to the lower atmosphere between 25 and 30 km, while regional and global events have risen to altitudes ~70 km. This dust cloud can be transported from the lower to upper atmosphere through dynamical coupling processes providing expansion of the thermosphere and increased densities during the event. However, it should be noted that no dust storm activity was detected from September 1998 through February 1999 because MGS was in its second aerobraking maneuver between these periods. But full disc image of Mars have been taken in these periods by the Hubble Space Telescope (see Web site http://www.astroleague.org/marswatch/). They show a water ice cloud belt near 80°E longitude. This cloud developed at afternoon local times at low northern latitude between altitudes from 10 to 70 km during northern spring in December 1998, when ACC measured mass densities. In this region the optical depth was about 0.6 to 0.7, which is significantly large. Therefore, the measured density at low latitudes could have increased near 80°E relative to other longitudes. The other possibility for enhanced thermosphere density at this longitude could be related to the Hadley circulation, which appears between 60°E and 110°E on the eastern-western slopes of Syrtis Major. During summer

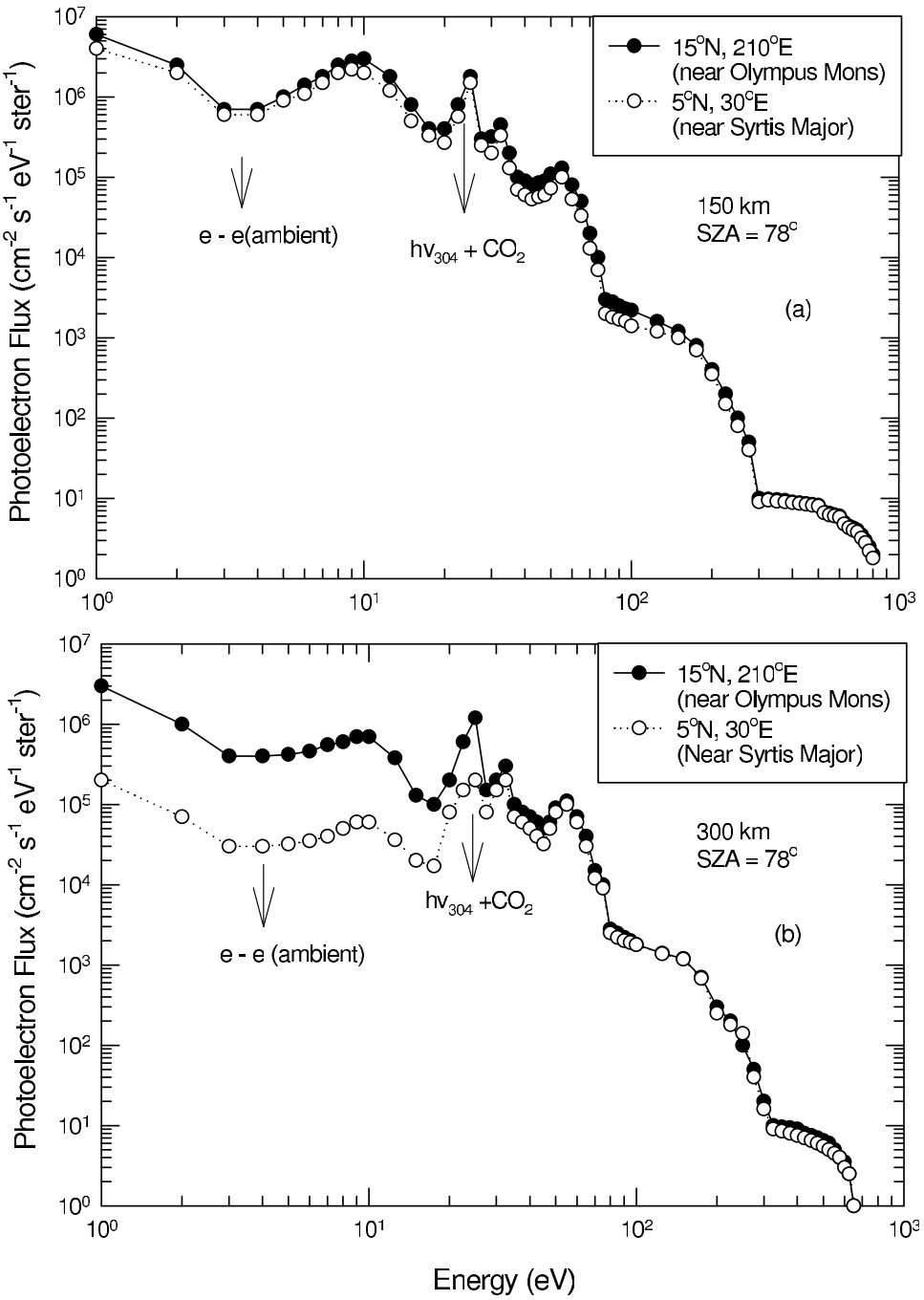

Figure 7. The photoelectron flux energy spectra at (a) 150 km and (b) 350 km in the Martian ionosphere over Olympus Mons and Syrtis Major.

season the solar insolation would be greatest on Mars at low latitudes. Therefore the Hadley circulation may be pumping atmospheric dust high into atmosphere.

[14] MTGCM is a three-dimensional model that has been used successfully by *Bougher et al.* [2000] to address the Mars upper atmospheric structure and dynamics above ~70 km. This model solves a finite difference primitive equation that self-consistently calculates neutral, ion, and electron densities over the globe under solar minimum, moderate, and maximum conditions at different Mars seasons. The prognostic equation for neutral species CO_2, N_2, O_2, O, and CO and ionic species O_2^+, CO_2^+, and O^+ were included in this model under a photoequilibrium condition. Zonal, meridional, and vertical velocities, temperatures, and geopotential heights were also obtained on 33 pressure levels (above 1.32 μbar) corresponding to ~70–300 km with a 5° latitude and longitude resolution. The vertical coordinate is log-pressure with a vertical spacing of two grid points per scale height. Adjustable parameters that can be varied for individual MTGCM cases include the $f_{10.7}$ index (solar X-ray/EUV/UV flux variation), heliocentric distance (orbital variation), solar declination (seasonal variation), and

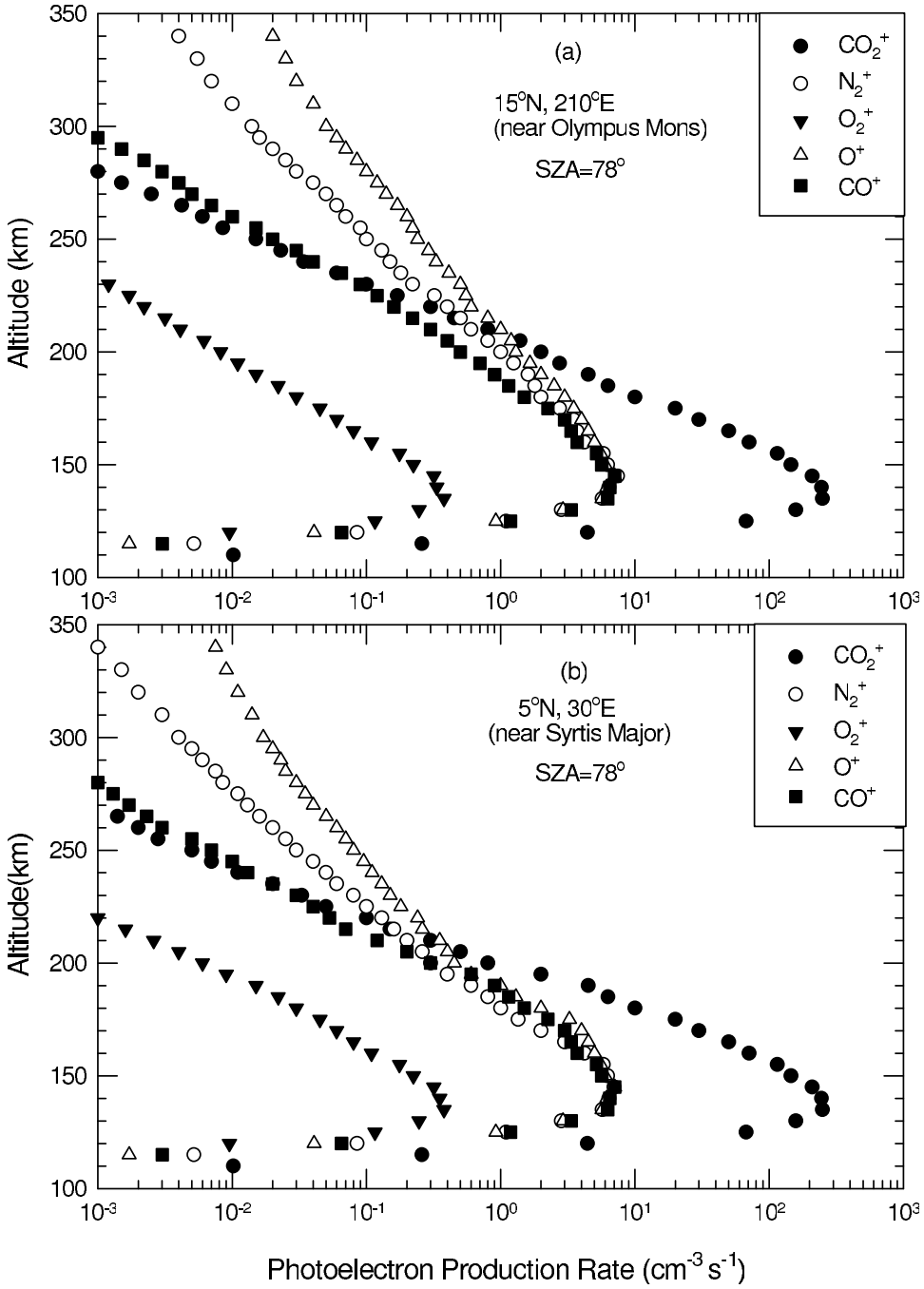

Figure 8. The photoelectron impact ionization rates of gases CO_2^+, N_2^+, O_2^+, O^+, and CO^+ in the Martian ionosphere over (a) Olympus Mons and (b) Syrtis Major.

the maximum eddy coefficient for eddy diffusion and viscosity. The MTGCM is also modified to accommodate atmospheric inflation and semidiurnal/diurnal tidal mode amplitudes and phases consistent with dusty conditions present in Mars lower atmosphere during dust storm events [*Bougher et al.*, 1999]. In the present paper, this code is used to calculate the neutral densities of gases CO_2, N_2, O_2, O, and CO at two latitudes (2.5°N and 22.5°N) and nine east longitudes (0°E, 45°E, 90°E, 135°E, 180°E, 225°E, 270°E, 315°E, and 360°E). This calculation is carried out in the month of December 1998 during MGS-phase 2 aerobraking period. At that time Mars experienced northern summer (Ls = 90) with moderate solar activity condition ($f_{10.7}$ = 124). The calculated density of CO_2 is used for comparison with the ACC data obtained from MGS at the same location. We have found reasonable agreement between MTGCM results and measurements at all longitudes except ~80°E, where the modeled densities are smaller by factor of 2.5 to 3 than the measurements. This difference is possibly due to the presence of a local dust storm providing expansion of the entire densities from lower to upper atmosphere as described above. This enhancement in the calculated density is not

Table 1. The Photoelectron Fluxes at 300 km

E(eV)	Olympus Mons (Local Loss Model)	Syrtis Major (Transport Model)
1.0	3.0×10^6	2.0×10^5
5.0	4.2×10^5	3.2×10^4
10.0	7.0×10^5	6.0×10^4
15.0	1.3×10^5	2.0×10^4
20.0	2.0×10^5	8.0×10^4
25.0	1.2×10^6	2.0×10^5
30.0	2.0×10^5	1.5×10^5
40.0	7.0×10^4	5.0×10^4
50.0	9.0×10^4	8.0×10^4
60.0	7.0×10^4	6.0×10^4
70.0	1.5×10^4	1.2×10^4
80.0	2.8×10^3	2.5×10^3
90.0	2.2×10^3	2.0×10^3
100.0	1.8×10^3	1.78×10^3
150.0	1.2×10^3	1.18×10^3
200.0	3.0×10^2	2.5×10^2
300.0	2.0×10^1	1.6×10^1
400.0	9.0	7.5
500.0	6.5	5.5
600.0	3.5	3.0
700.0	0.6	0.55
800.0	0.20	0.19
900.0	0.09	0.08
1000.0	0.07	0.06

possible to reproduce by the MTGCM simulation because lower and upper atmospheric processes are not coupled in the model. The dust heats the lower atmosphere providing expansion of the entire densities with the progression of a dust storm. A single coupled chemically heated dynamical model can realistically address regional dust storm events at Mars [*Bougher et al.*, 1999]. It appears that the measured densities are dominated by wave harmonics. This is a short-term variation, which is also not produced by the MTGCM. In this model planetary waves, tidal and gravity waves must be properly incorporated and passed from the lower to upper atmosphere in order to explain short term thermospheric variation monitored throughout aerobraking.

5. Results and Discussion

[15] We have represented our calculated photoelectron flux and ion production rates in Figures 7 and 8, respectively. The photoelectron fluxes are calculated in the regions of Olympus Mons and Syrtis Major at altitudes of 150 km and 300 km at energies from 1 to 1000 eV. We report that major characteristics of the photoelectron spectra are produced by model calculations. It is found that the photoelectron spectrum falls of exponentially with increasing energy due to a rapid decrease of solar flux and photoionization cross sections at short wavelengths. The photoelectrons dominate the electron spectrum below 90 eV. The first peak near 25–27 eV is obtained due to absorption of He II Lyman α line at 304 Å as reported by *Mantas* and *Hanson* [1979] and *Fox and Dalgarno* [1979]. The second major peak that was noted by these authors is not found at these energies due to our choice of energy intervals of 2.5 eV. The sharp drop at about 300 eV and 800 eV are found due to low values of X-ray fluxes at these energies [*Tobiska et al.*, 2000]. The photoelectron flux around this energy range is highly dependent on solar flux of X-ray irradiance that is dominated by coronal emission lines. The intensity of these lines can vary by factors of several over short-term periods. The valleys around 3 eV are due to energy loss by electron-ambient electron collision. We have incorporated this process by adding a term $n_e(z)\ \sigma_{e\text{-}e}(E)$ in the summation appearing in the denominators of equations (4) and (11). Here $n_e(z)$ is the electron density and $\sigma_{e\text{-}e}(E)$ is effective electron-ambient electron collision cross section [*Bhardwaj et al.*, 1990]. The model results do not show Auger peaks of C, N, and O at an energy range between 200 eV and 500 eV as pointed out by MGS [*Mitchell et al.*, 2000] due to choice of our large energy intervals of 25 eV. The photoelectron fluxes do not change significantly over the two regions at altitude 150 km (Figure 7a). The transport of photoelectrons is appreciable only above 250 km. At altitude 300 km, the photoelectron flux is reduced by an order of magnitude between energy 1 to 20 eV due to transport compared to local losses alone (Figure 7b). The transport of photoelectrons does not contribute significantly at lower altitudes where the mean free path is smaller then the scale height (~23 km). Therefore, it is necessary to take into account the effects of vertical magnetic fields at high altitude in the atmosphere above Syrtis Major due to very large mean free paths of photoelectrons. In the three-dimensional transport model the effect of transport on photoelectron fluxes is clearly evident at high altitude. The photoelectron fluxes at 300 km are given in Table 1 for Syrtis Major and Olympus Mons at a few selected energies. In Figures 8a and 8b, we represent the calculations of production rates of five ions (CO_2^+, N_2^+, O_2^+, O^+, and CO^+) at Olympus Mons and Syrtis Major by using two-dimensional and three-dimensional transport models, respectively. We note that there is no change between these two model calculations at altitude $\leq$200 km. Above this altitude the ion production rates at Syrtis Major are reduced by factors of 3–5 due to transport of photoelectrons. The maximum ionizations of CO_2^+, N_2^+, O_2^+, O^+, and CO^+ are found to be 2.45×10^2, 7.43, 3.7×10^{-1}, 7.0 and 7.1 $cm^{-3}\ s^{-1}$ at about 140, 137, 125, 141, and 139 km, respectively. The production of O^+ is greater than CO_2^+, N_2^+, O_2^+, and CO^+ above 200 km because atomic oxygen is the dominant gas there.

[16] In Figures 9a and 9b the photoionization rates are shown at Olympus Mons and Syrtis Major, respectively. The photoionization rates are obtained from the primary photoelectron spectrum $Q(h_o, E_o)$ by integrating it over energy E_o. The maximum photoionization rates of CO_2^+, N_2^+, O_2^+,O^+, and CO^+ are found to be 1.34×10^3, 5×10^1, 3.1, 4.7×10^1 and 3.5×10^1 $cm^{-3}\ s^{-1}$ at about 147 km, 143 km, 140 km, 149 km, and 145 km, respectively. These production rates do not change over the two regions. This is due to the fact that it is directly proportional to the neutral density (see equation (3)), which is changing insignificantly in the Martian atmosphere. Therefore, the calculated photo ion production rates will not change significantly at different locations of Mars. The differences in the production rates can be found at different solar zenith angles. As the solar zenith angle increases, the peak rises and the magnitude of the maximum production rate decreases by factors of 2 to 2.5 [cf. *Fox and Dalgarno*, 1979; *Fox and Yeager*, 2006]. In Figures 10 and 11 we have shown estimated profiles of ion

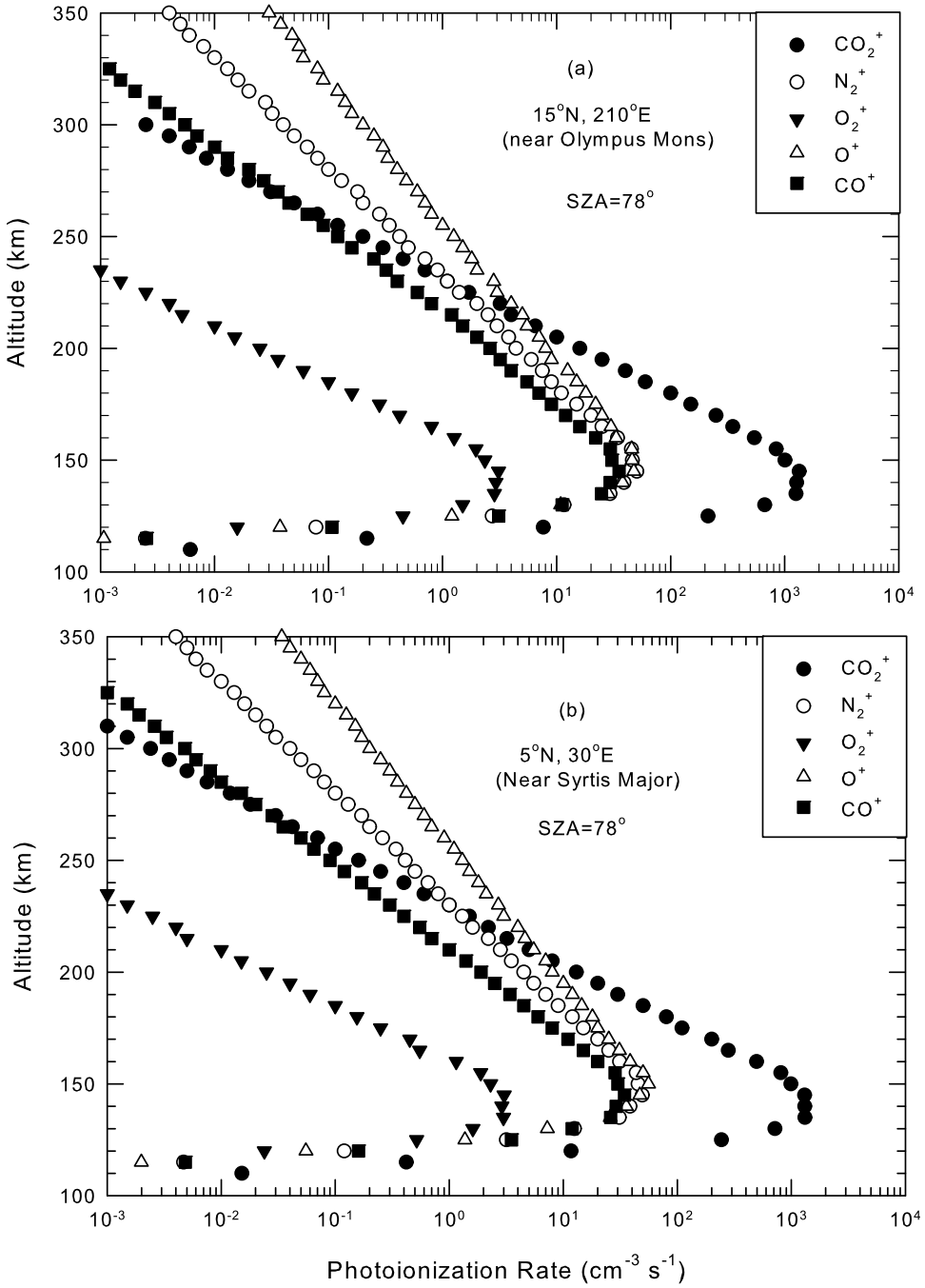

Figure 9. The photoionization rates of gases CO_2^+, N_2^+, O_2^+, O^+, and CO^+ in the Martian ionosphere over (a) Olympus Mons and (b) Syrtis Major.

and electron densities, respectively. For these calculations we have used one-dimensional continuity model as given by *Haider and Oyama* [2002]. This model is coupled with the production rates, loss rates, and flux divergence of the vertical momentum equation. This is a time-dependent model. It is solved by using a finite implicit method with lower and upper boundary conditions. The photochemical equilibrium condition is imposed on the ion densities at lower boundary (110 km) where the vertical velocity is set to zero. The vertical velocity at the upper boundary is set to be 1×10^5 cm/s corresponding to an upward mean flux of 5×10^7 cm^{-2} s^{-1} [cf. *Chen et al.*, 1978; *Fox and Yeager*, 2006].The chemical scheme, plasma temperature, ion and thermal diffusion coefficients are essentially the same as those used in our previous paper. In the one-dimensional model this flux represents the divergence of the horizontal flux of ions, which may be related to the interaction between the solar wind and the ionosphere [*Shinagawa and Cravens*, 1989; *Tanaka*, 1998; *Ma et al.*, 2004; *Lundin et al.*, 2006]. In this calculation the photoionization and photoelectron impact ionization rates are taken

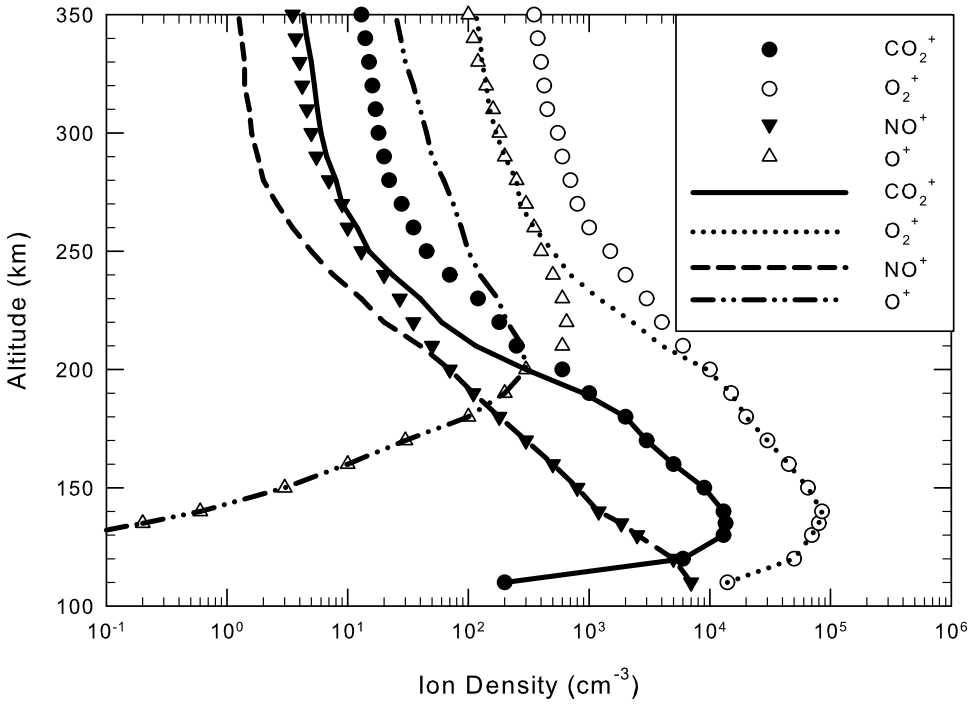

Figure 10. The estimated ion density profiles of CO_2^+, O_2^+, NO^+, and O^+ in the Martian the dayside ionosphere of Mars. The first four legends are shown for Olympus Mons while the last four legends are represented for Syrtis Major.

from Figures 8 and 9. The dynamics of the upper ionosphere of Mars is not known at low latitude due to lack of measurements of plasma velocity and electron density. Therefore, we have solved the one-dimensional continuity equation due to ambipolar diffusion using a fixed flux boundary condition appropriate at the ionopause of middle- to high-latitude ionosphere. *Ma et al.* [2004], *Ma and Nagy* [2007], and *Duru et al.* [2008] have used three-dimensional models to study

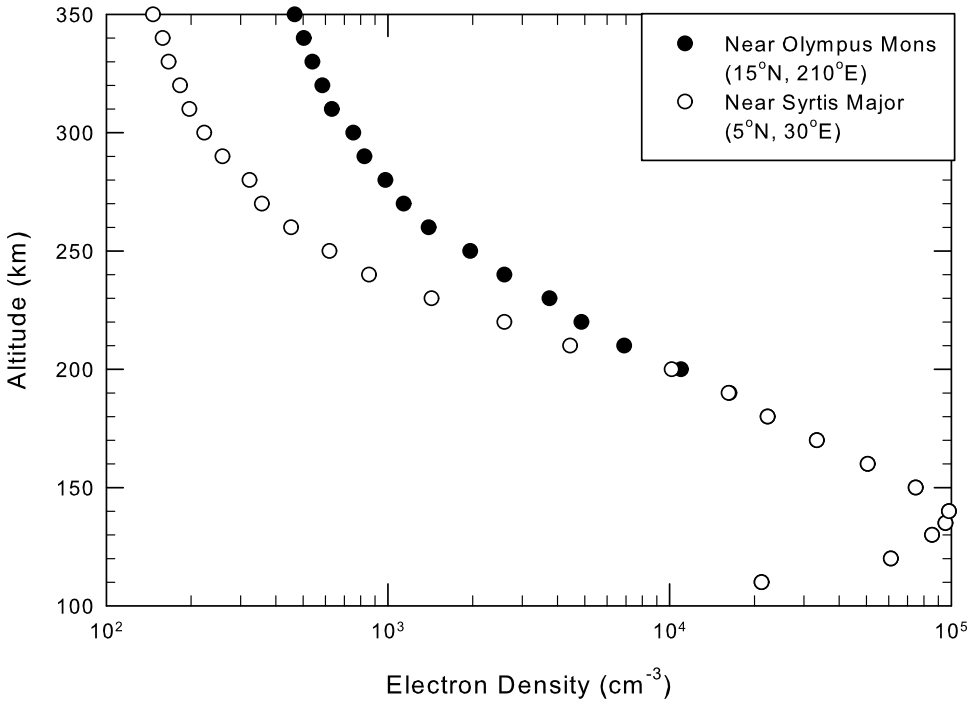

Figure 11. The estimated electron density profiles in the Martian ionosphere close to Olympus Mons and Syrtis Major.

the dynamics of the upper ionosphere of Mars at high latitude. Our predicted density can be changed by about 5% above 250 km due to variation in upper boundary conditions during the periods of strong solar wind pressure. Including the dynamics of the solar wind is beyond the scope of this paper.

[17] The photoionization and photoelectron impact ionization have produced a major ion CO_2^+ that is quickly removed by atomic oxygen leading to O_2^+ as the dominant ion. Therefore, CO_2^+ is not produced significantly in the Martian ionosphere. The loss of O_2^+ with NO is a major source of NO^+ (the neutral density of NO in the chemistry is taken from *Fox* [1993]). These ions are entirely destroyed by the dissociative recombination process. The production of O^+ is quite abundant in the upper atmosphere. This ion is mostly destroyed by CO_2. This is a very fast reaction to permit the development of a significant layer of O_2^+. MGS has observed mean *F*-peak electron densities $\sim 8.4 \times 10^4$ cm^{-3} at high latitude from a radio occultation experiment [*Haider et al.*, 2009]. Under local equilibrium conditions between the ion production rate and O_2^+ dissociative recombination the peak electron density in the dayside ionosphere at low latitude can be estimated as $N_e = \mathrm{sqrt}(q/\alpha)$, where $\alpha = 1.9 \times 10^{-7}\ (300/T_e)^{0.5}$ cm^3 s^{-1} [*Mul and McGowan*, 1979] and q represents the production rates of CO_2^+ from the photoionization and photoelectron impact ionization. The total peak production rate (peak photoionization rate + peak photoelectron production rate) of CO_2^+ is calculated as $\sim 1.6 \times 10^3$ cm^{-3} s^{-1}. By putting the value of total production rates of CO_2^+ in the above equation, we get the maximum electron density $N_e \sim 9 \times 10^4$ cm^{-3}, which is nearly equal to the estimated electron density at altitude ~144 km (see Figure 11). There is no significant difference in the peak electron density between the ionospheres at low and high latitudes. This is due to the fact that neutral densities are nearly the same in the Martian atmosphere at low and high latitudes. As expected the ion and electron densities are reduced by factors of ~3 above 200 km due to transport of photoelectrons at Syrtis Major. The difference between the ion/electron densities at Syrtis Major and Olympus Mons is less extreme than the difference in their photoelectron flux and photoelectron production rates. This is because photoionization rates do not change significantly between the two locations. The photoelectron impact ionization rates contribute only ~30% to the electron density. Below 200 km, there is no effect of photoelectron transport in the ionosphere of Mars. The electron density decreases nearly exponentially from the peak altitude to about 200 km, which is the bottom of the diffusive equilibrium region [cf. *Haider and Oyama*, 2002]. It should be noted that our calculated results can also be used at other locations because the atmosphere of Mars is mixed with crustal and solar wind fields throughout the globe in absence of planetary magnetic fields and the neutral density is not changing much at different places. The present calculations are made in the Martian atmosphere over the two regions, which are representative of horizontal and vertical magnetic fields.

6. Conclusion

[18] We have calculated photoelectron flux, production rates, and ion/electron densities in the ionosphere of Mars at Syrtis Major (5°N, 30°E) and Olympus Mons (15°N, 210°E) in the presence of vertical and horizontal magnetic fields by using a two-dimensional yield spectrum (local loss model) and a three-dimensional yield spectrum (transport model), respectively. Between 110 km and 160 km, we have constructed neutral density model atmospheres over these regions from MGS/ACC data. Above this height the neutral density is taken from *Bougher et al.* [2000] and *Fox* [1997]. These calculations are made at SZA 78° during medium solar activity condition. It is found that the transport of photoelectrons is appreciable above 200 km. The photoelectron transport reduces the flux and ion production rates at Syrtis Major by factors of 3 to 10 as compared to the local loss calculation carried out at Olympus Mons. The ion and electron density are also reduced by in the upper ionosphere of Syrtis Major from the Olympus Mons by a factor of ~2.5 due to transport of photoelectrons. Below this height they are decreasing exponentially up to the maximum peak altitude. For this calculation we have used a one-dimensional continuity diffusion (vertical) model. The physics of the middle- and high-latitude ionospheres have been described from the results of past radio science observations of the ionosphere of Mars [cf. *Nagy et al.*, 2004; *Withers*, 2009]. But little is known of the low-latitude ionosphere. Our effort deals with this largely unmeasured region. The challenge for the future is to develop theories and experiments to study the dynamics of the low-latitude ionosphere. Therefore, it is necessary to evaluate opportunities for obtaining observations at low-latitude regions. The physics of the low-latitude ionosphere should be very much different from the middle- and high-latitude ionospheres similar to differences discovered in the Earth's ionosphere from the satellite and ground-based observations. In the absence of ionospheric measurements at low latitude our results provide benchmark values that may help to guide the design of future ionospheric payloads to measure and confirm the effects of photoelectron transport and its influence on the dynamics of the upper ionosphere of Mars.

[19] **Acknowledgments.** The authors are thankful to MGS science team and NASA's Planetary Data System for providing us accelerometer data. S. P. Seth thanks University Grant Commission (UGC), India, for the support through a research project no. 47-255/07.

[20] Masaki Fujimoto thanks Anil Bhardwaj and another reviewer for their assistance in evaluating this paper.

References

Acuna, M. H., et al. (1998), Magnetic field and plasma observations at Mars: Initial results of the Mars Global Surveyor Mission, *Science*, *279*, 1676–1680.

Bhardwaj, A., and S. K. Jain (2009), Monte Carlo model of electron energy degradation in a CO_2 atmosphere, *J. Geophys. Res.*, *114*, A11309, doi:10.1029/2009JA014298.

Bhardwaj, A., S. A. Haider, and R. P. Singhal (1990), Auroral and photoelectron fluxes in cometary ionospheres, *Icarus*, *85*, 216–228.

Bougher, S. W., S. Engel, R. G. Roble, and B. Foster (1999), Comparative terrestrial planet thermospheres, 2. Solar cycle variation of global structure and winds at equinix, *J. Geophys. Res.*, *104*(E7), 16,591–16,611.

Bougher, S. W., S. Engel, R. G. Roble, and B. Foster (2000), Comparative terrestrial planet thermospheres, 3, Solar cycle variation of global structure and winds at solstices, *J. Geophys. Res.*, *105*(E7), 17,669–17,692.

Brain, D. A., F. Bagenal, M. H. Acuna, and J. E. P. Connerney (2003), Martian magnetic morphology contributions from the solar wind and crust, *J. Geophys. Res.*, *108*(A12), 1424, doi:10.1029/2002JA009482.

Cain, J. C., B. B. Ferguson, and D. Mozzoni (2003), An $n = 90$ internal potential function of the Martian crustal magnetic field, *J. Geophys. Res.*, *108*(E2), 5008, doi:10.1029/2000JE001487.

Cantor, B. A., P. B. James, M. Caplinger, and M. J. Wolf (2001), Martian dust storms: 1999 Mars orbiter camera observations, *J. Geophys. Res.*, *106*(E10), 23,653–23,688.

Chen, R. H., T. E. Cravens, and A. F. Nagy (1978), The Martian ionosphere in light of Viking observations, *J. Geophys. Res.*, *83*(A8), 3871–3876.

Connerney, J. E. P., et al. (1999), Magnetic lineations in the ancient crust of Mars, *Science*, *284*, 794–798.

Connerney, J. E. P., M. H. Acuna, N. F. Ness, G. Kletetschka, D. L. Mitchell, R. P. Lin, and H. Reme (2005), Tectonic implications of Mars crustal magnetism, *Proc. Natl. Acad. Sci.*, *102*(42), 14970–14975.

Dolginov, S. S. (1978a), On the magnetic field of Mars: Mars 2 and 3 evidence, *Geophys. Res. Lett.*, *5*(1), 89–92, doi:10.1029/GL005i001p00089.

Dolginov, S. S. (1978b), On the magnetic field of Mars: Mars 5 evidence, *Geophys. Res. Lett.*, *5*(1), 93–95, doi:10.1029/GL005i001p00093.

Dolginov, S. S., Y. G. Yeroshenko, and L. N. Zhuzgov (1973), Magnetic field in the very close neighborhood of Mars according to data from Mars 2 and Mars 3 spacecraft, *J. Geophys. Res.*, *78*(22), 4779–4786.

Duru, F., D. A. Gurnett, D. D. Morgan, R. Modolo, A. F. Nagy, and D. Najib (2008), Electron densities in the upper ionosphere of Mars from the excitation of electron plasma oscillations, *J. Geophys. Res.*, *113*, A07302, doi:10.1029/2008JA013073.

Fjeldbo, G., W. C. Fjeldbo, and V. R. Eshleman (1966), Atmosphere of Mars: Mariner 4 models compared, *Science*, *153*, 1518–1523.

Fjeldbo, G., A. Kliore, and B. Seidel (1970), The Mariner 1969 occultation measurements of the upper atmosphere of Mars, *Radio Sci.*, *5*(2), 381–386.

Fjeldbo, G., D. Sweetnam, J. Brenkle, E. Christensen, D. Farless, J. Mehta, B. Seidel, W. Michael, A. Wallio, and M. Grossi (1977), Viking radio occultation measurements of Martian atmosphere and topography: Primary mission coverage, *J. Geophys. Res.*, *82*(28), 4317–4324.

Fox, J. L. (1993), The production and escape of nitrogen atoms on Mars, *J. Geophys. Res.*, *98*(E2), 3297–3310.

Fox, J. L. (1997), Upper limits to the outflow of ions at Mars: Implications for atmospheric evolution, *Geophys. Res. Lett.*, *24*(22), 2901–2904, doi:10.1029/97GL52842.

Fox, J. L., and A. Dalgarno (1979), Ionization, luminosity and heating of the upper atmosphere of Mars, *J. Geophys. Res.*, *84*(A12), 7315–7331.

Fox, J. L., and K. E. Yeager (2006), Morphology of the near terminator Martian ionosphere: A comparison of models and data, *J. Geophys. Res.*, *111*, A10309, doi:10.1029/2006JA011697.

Frahm, R. A., et al. (2006), Carbon dioxide photoelectron energy peaks at Mars, *Icarus*, *182*, 371–382.

Green, A. E. S., C. H. Jackman, and R. H. Garvey (1977), Electron impact on atmospheric gases, 2. Yield spectra, *J. Geophys. Res.*, *82*(32), 5104–5111.

Haider, S. A., and K. I. Oyama (2002), Calculated electron flux and densities at 10–1000 eV in the dayside Martian ionosphere: Composition with MGS and Viking results, *Indian J. Radio. Space Phys.*, *31*, 173–182.

Haider, S. A., and R. P. Singhal (1983), Analytical yield spectrum approach to electron energy degradation in Earth's atmosphere, *J. Geophys. Res.*, *88*(A9), 7185–7189.

Haider, S. A., and R. P. Singhal (1986), Analytical approach to backscattering of low energy electrons, *J. Geophys. Res.*, *91*(A12), 13761–13763.

Haider, S. A., V. Singh, V. R. Choksi, W. C. Maguire, and M. I. Verigin (2007), Calculated densities of $H_3O^+(H_2O)_n$, $NO_2^-(H_2O)_n$, $CO_3^-(H_2O)_n$ and electron in the nighttime ionosphere of Mars: Impact of solar wind electron and galactic cosmic rays, *J. Geophys. Res.*, *112*, A12309, doi:10.1029/2007JA012530.

Haider, S. A., M. A. Abdu, I. S. Batista, J. H. Sobral, Xiaoli Luan, Esa Kallio, W. C. Maguire, M. I. Verigin, and V. Singh (2009), D, E, and F layers in the daytime at high latitude terminator ionosphere of Mars: Comparison with Earth's ionosphere using COSMIC data, *J. Geophys. Res.*, *114*, A03311, doi:10.1029/2008JA013709.

Hinson, D. P., R. A. Simpson, J. D. Twicken, and G. L. Tyler (1999), Initial results from radio occultation measurements with Mars Global Surveyor, *J. Geophys. Res.*, *104*(E11), 26,997–27,012.

Keating, G. M., et al. (1998), The structure of the upper atmosphere of Mars: In situ accelerometer measurements from Mars Global Surveyor, *Science*, *279*, 1672–1676.

Kliore, A. J., D. L. Cain, G. S. Levy, V. R. Eshleman, G. Fjeldbo, and F. O. Drake (1965), Occultation experiment: Results of the first direct measurements of Mars atmosphere and ionosphere, *Science*, *149*, 1243–1248.

Kliore, A. J., D. L. Cain, G. Fjeldbo, B. L. Seidel, M. J. Sykes, and S. I. Rasool (1972), The atmosphere of Mars from Mariner 9 radio occultation measurements, *Icarus*, *17*, 484–516.

Kliore, A. J., G. Fjeldbo, B. L. Seidel, M. J. Sykes, and P. M. Woiceshyn (1973), S band radio occultation measurements of the atmosphere and topography of Mars with Mariner 9: Extended mission coverage of polar and intermediate latitudes, *J. Geophys. Res.*, *78*(20), 4331–4351.

Kolosov, M. A., V. M. Ivanov, D. S. Lukin, and Y. G. Spiridonov (1976), Radio occultation of the Martian ionosphere taking into account horizontal gradients of electron density, *Space Res.*, *16*, 1013–1017.

Lillis, R. J., D. L. Mitchell, R. P. Lin, J. E. P. Connerney, and M. H. Acuna (2004), Mapping crustal magnetic fields at Mars using electron reflectometry, *Geophys. Res. Lett.*, *31*, L15702, doi:10.1029/2004GL020189.

Lundin, R., et al. (2006), Ionospheric plasma acceleration of Mars: ASPERA 3 results, *Icarus*, *182*, 308–319.

Ma, Y.-J., and A. F. Nagy (2007), Ion escape fluxes from Mars, *Geophys. Res. Lett.*, *34*, L08201, doi:10.1029/2006GL029208.

Ma, Y.-J., A. F. Nagy, I. V. Sokolov, and K. C. Hansen (2004), Three dimensional, multispecies, high spatial resolution MHD studies of the solar wind interaction with Mars, *J. Geophys. Res.*, *109*, A07211, doi:10.1029/2003JA010367.

Mantas, G. P., and W. B. Hanson (1979), Photoelectron fluxes in the Martian ionosphere, *J. Geophys. Res.*, *84*(A2), 369–385.

Mitchell, D. L., et al. (2000), Oxygen Auger electrons observed in mars ionosphere, *Geophys. Res. Lett.*, *27*(13), 1871–1874, doi:10.1029/1999GL010754.

Mitchell, D. L., R. J. Lillis, R. P. Lin, J. E. P. Connerney, and M. H. Acuna (2007), A global map of Mars' crustal magnetic field based on electron reflectometry, *J. Geophys. Res.*, *112*, E01002, doi:10.1029/2005JE002564.

Mul, P. M., and J. W. McGowan (1979), Temperature dependence of dissociative recombination for atmospheric ions NO, O_2, N_2, *J. Phys. B*, *12*, 1591–1602.

Nagy, A. F., et al. (2004), The plasma environment of Mars, *Space Sci. Rev.*, *111*(1), 33–114.

Patzold, M., S. Tellmann, B. Hausler, D. Hinson, R. Schaa, and G. L. Tyler (2005), A sporadic third layer in the ionosphere of Mars, *Science*, *310*, 837–838.

Riedler, W., et al. (1989), Magnetic field near Mars: First results, *Nature*, *341*, 604–607.

Savich, N. A., and V. A. Samovol (1976), The night time ionosphere of Mars from Mars 4 and Mars 5 dual frequency radio occultation measurements, *Space Res., XVI*, 1009–1010.

Seth, S. P., S. A. Haider, and K. I. Oyama (2002), Photoelectron flux and nightglow emission of 5577 Å and 6300 Å due to solar wind electron precipitation in the Martian atmosphere, *J. Geophys. Res.*, *107*(A10), 1324, doi:10.1029/2001JA000261.

Seth, S. P., U. B. Jayanthi, and S. A. Haider (2006a), Estimation of peak electron density in the upper ionosphere of Mars at high latitude (50o–70oN) using MGS /ACC data, *Geophys. Res. Lett.*, *33*, L19204, doi:10.1029/2006GL027064.

Seth, S. P., V. B. Rao, C. M. Espirto Santo, S. A. Haider, and V. R. Choksi (2006b), Zonal variation of peak ionization rates in upper atmosphere of Mars at high latitude using Mars Global Surveyor Accelerometer data, *J. Geophys. Res.*, *111*, A09308, doi:10.1029/2006JA011753.

Shinagawa, H., and T. E. Cravens (1989), A one dimensional multispecies magnetohydrodynamic model of the dayside ionosphere of Mars, *J. Geophys. Res.*, *94*(A6), 6506–6516.

Shinagawa, H., and T. E. Cravens (1992), The ionospheric effects of a weak intrinsic magnetic field at Mars, *J. Geophys.Res.*, *97*(E1), 1027–1035.

Singhal, R. P., and A. E. S. Green (1981), Spatial aspects of electron energy degradation in atomic oxygen, *J. Geophys. Res.*, *86*(A6), 4776–4780.

Singhal, R. P., and S. A. Haider (1984), Analytical yield spectrum approach to photoelectron fluxes in the Earth's atmosphere, *J. Geophys. Res.*, *89*(A8), 6847–6852.

Singhal, R. P., C. H. Jackman, and A. E. S. Green (1980), Spatial aspects of low- and medium-energy electron degradation in N_2, *J. Geophys. Res.*, *85*(A3), 1246–1254.

Smith, E. J., L. Davis, P. Coleman, and D. E. Jones (1965), Magnetic field measurements near Mars, *Science*, *149*, 1241–1242.

Snyder, C. W., and V. I. Moroz (1992), Spacecraft exploration of Mars, in *Mars*, edited by H. H. Kieffer, B. M. Jakosky, C. W. Snyder, and M. S. Matthews, p. 71–119, University of Arizona Press, Tuscon.

Tanaka, T. (1998), Effects of decreasing ionospheric pressure on the solar wind interaction with non-magnetized planets, *Earth Planets Space*, *50*, 259–265.

Tobiska, W. K., T. Woods, F. Eparvier, R. Viereck, L. Floyd, D. Bouwer, G. Rottman, and O. R. White (2000), The SOLAR 2000 empirical solar irradiance model and forecast tool, *J. Atmos. Sol. Terr. Phys.*, *62*, 1233–1250.

Tyler, G. L., G. Balmini, D. P. Hinson, W. L. Sjogren, D. E. Smith, R. A. Simpson, S. W. Asmar, P. Priest, and J. D. Twicken (2001), Radio science

observations with Mars Global Surveyor: Orbit insertion through one Mars year in mapping orbit, *J. Geophys. Res.*, *106*(E10), 23,327–23,348.
Vasiliev, M. B., et al. (1975), Preliminary results of dual frequency radio occultation of the Martian ionosphere with the aid of Mars 5 spacecraft in 1974 (in Russian), *Kosm, Issled*, *13*, 48–51.
Withers, P. (2009), Areview of observed variability in the dayside ionosphere of Mars, *Adv. Space Res.*, *44*, 277–307.

S. W. Bougher, Department of Atmospheric, Oceanic and Space Sciences, University of Michigan, 2455 Hayward St., Ann Arbor, MI 48109, USA.

D. A. Brain and D. L. Mitchell, Space Sciences Laboratory, University of California, 7 Gauss Way, Berkeley, CA 94720, USA.

S. A. Haider, Space and Atmospheric Sciences, Physical Research Laboratory, Navarangpura, Ahmedabad, 380009, India. (haider@prl.res.in)

T. Majeed, Department of Physics, American University of Sharjah, PO Box 26666, Sharjah, UAE.

S. P. Seth, Department of Physics, Bhavan's R. A. College of Science, Gujarat University, Ahmedabad 380001, India.